Geothermal Energy

RESEARCH Open Access

Parameter identification and range restriction through sensitivity analysis for a high-temperature heat injection test

Stefan Heldt[1*], Bo Wang[1,2,3] and Sebastian Bauer[1,2]

*Correspondence:
stefan.heldt@ifg.uni-kiel.de

[1] Institute of Geosciences, Christian-Albrechts-University Kiel, Ludewig-Meyn-Str. 10, 24118 Kiel, Germany
[2] Kompetenzzentrum Geo-Energie of Kiel University (KGE), Christian-Albrechts-University Kiel, Ludewig-Meyn-Str. 10, 24118 Kiel, Germany
[3] Present Address: M&P ENERGY GmbH, Sachsenstraße 6, 20097 Hamburg, Germany

Abstract

In order to compensate for the variable mismatch between heat demand and heat production from renewable sources or waste heat, high-temperature aquifer thermal energy storage (HT-ATES) is a promising option. A reliable prediction of the energetic performance as well as thermal and hydraulic impacts of a HT-ATES requires a suitable model parameterization regarding the subsurface properties. In order to identify the subsurface parameters on which investigation efforts should be focused, we carried out an extensive sensitivity analysis of the thermal and hydraulic parameters for a high-temperature heat injection test (HIT) using numerical modeling of the governing coupled thermo-hydraulic processes. The heat injection test was carried out in a quaternary shallow aquifer using injection temperatures of about 75 °C over 5 days, accompanied by an extensive temperature monitoring. The sensitivity analysis is conducted for parameter ranges based on literature values, based on site investigation at the HIT site and based on a model calibrated to the measured temperature distribution following the heat injection. Comparing the parameter ranges thus obtained in this three-step approach allows to identify those parameters, for which model prediction uncertainty decreased most, which are also the parameters, that strongly affect the thermal behavior. The highest sensitivity is found for vertical and horizontal hydraulic conductivity as well as for groundwater flow velocity, indicating that investigation efforts for HT-ATES projects should focus on these parameters. Heat capacity and thermal conductivity have a smaller impact on the temperature distribution. Our work thus yields a consistent approach to identifying the parameters which can be best restricted by field investigations and subsequent model calibration. Focusing on these during field investigations thus enable improved model predictions of both HT-ATES operation and induced impacts.

Keywords: High-temperature heat injection test, Sensitivity analysis, Numerical modeling, OpenGeoSys, Aquifer thermal energy storage, Parameter investigation

Introduction

The aims of countries and companies to reduce greenhouse gas emissions in order to counteract global warming, entail the large-scale application of renewable energy technologies. The heating sector has a particular relevance in this context, since it accounts

for about 50% of the primary energy consumption worldwide (REN21 2016). In order to tackle the seasonal mismatch between heat demand in winter and supply by renewable solar sources mainly in summer or from waste heat, seasonal thermal energy storage is required. One promising storage option is Aquifer Thermal Energy Storage (ATES), for which water is extracted from an aquifer using a well, heated during the heat injection phase using a heat exchanger, and reinjected through a second well back into the aquifer. During the heat extraction phase, the cycle is reversed, i.e., the warm water is pumped back to the surface, the stored heat is extracted at the heat exchanger and the cooled water is reinjected back into the aquifer using the other well. While most ATES systems operate with storage temperatures <40 °C (Fleuchaus et al. 2018), High-temperature-ATES (HT-ATES) uses increased temperatures of >50 °C. This yields the benefit of higher storage capacities (Dinçer and Rosen 2011) and no or less heat pumping being required for heating purposes. With the high temperatures, however, density-driven buoyancy flow in the aquifer can be induced (Molz et al. 1983), which is caused by the lower density of the injected hot water compared to the cool ambient groundwater (Krol et al. 2014; Nield and Bejan 2013) and can result in higher thermal losses because of an unequal vertical distribution of the heat in the storage formation (Schout et al. 2014). Suitable subsurface conditions for an efficient ATES operation are thus the occurrence of an approximately homogeneous aquifer with a medium to high hydraulic conductivity to allow for the required pumping rates but restrict heat loss by thermal convection (e.g., Nielsen and Vangkilde-Pedersen 2019) as well as low groundwater flow velocities (e.g., Bloemendal and Hartog 2018). Thus, especially for HT-ATES, reliable site-specific knowledge of geohydraulic subsurface conditions is required.

For ATES systems operating on all temperature ranges, a reliable prediction of storage characteristics, like heat recovery, thermal losses and return flow temperatures, as well as the thermally induced effects and impacts on the subsurface is thus required (Bauer et al. 2017; Kabuth et al. 2017; Meng et al. 2019), in order to guarantee the long-term and sustainable employment. Numerical models are therefore widely used for the dimensioning and energetic assessment of ATES and HT-ATES plants (Bridger and Allen 2010; Visser et al. 2015). A reliable prediction of thermal impacts is especially required for planning HT-ATES systems, since regulatory permission and connected subsurface space-planning issues depend on it. The predictive quality of numerical HT-ATES models depends on the quality of site-specific model parameterization. While some subsurface parameters vary over several orders of magnitude for similar sedimentary settings, other parameters are less variable. Hence it is important to know, for which parameters site-specific estimations are needed most, in order to obtain those systematically also in future HT-ATES projects. The most important parameters are those, which have the most pronounced influence on the thermal transport processes and thus the thermal efficiency and the induced impacts of HT-ATES systems. These parameters can be identified by sensitivity analysis using numerical models. In this study, therefore, we investigate the effects of parameters, for which well-established hydrogeological measuring techniques exist, which are the horizontal and vertical hydraulic conductivities, specific storage, groundwater flow velocity, thermal conductivity and volumetric heat capacity. Numerical studies on HT-ATES so far have shown that of these parameters, thermal efficiency of an ATES is most dependent on vertical and horizontal hydraulic conductivity,

but also depends on groundwater flow velocity, thermal conductivity and volumetric heat capacity (Gao et al. 2019; Jeon et al. 2015; Schout et al. 2014; Sheldon et al. 2021).

Typically, these parameters can be obtained by using hydrogeological field investigation methods. However, these parameters may vary spatially at a specific site, and their determination may thus be uncertain, especially if determination is based on point measurements. As Palmer et al. (1992) and Molson et al. (1992) as well as Heldt et al. (2021a) have shown, using a systematic field investigation strategy can lead to satisfying predictions of the long-term temperature evolution of a heat injection test (HIT). However, this does not allow for an assessment of the possible parameter ranges, the parameter uncertainty as well as the determination of an optimal set of parameters. To improve the reliability of the HT-ATES model further, the data obtained during a field test at the scale of the later application can be used to restrict parameter ranges further. This would reduce parameter uncertainty and increase model reliability further.

While thus the important parameters for a reliable prediction have been identified in the literature, parameter ranges of those may be large, causing uncertainty in model predictions. However, a site-specific parameter sensitivity study for HT-ATES or HT-HIT has not been reported in the literature. Also, no demonstration of model improvement by calibration to measured temperatures has been performed for HT-HIT. Therefore, in this paper, we examine the sensitivity of the thermal behavior induced by a HT-HIT to the hydraulic and thermal subsurface parameters. For this, model results obtained using parameter ranges from literature, from site-specific investigation and from model calibration are compared in a three-step approach to the measured temperature data, in order to quantify the data worth and the prediction quality of the individual parameters. For this, a specifically designed high-temperature heat injection test was performed in a shallow near-surface aquifer and used as a reference for parameter determination at the field scale as well as temperature sampling. This allows to identify the parameters whose ranges can be constrained the most and are thus essential for an accurate prediction of the thermal effects and the ensuing spatio-temporal temperature distribution. These in turn are the parameters on which site investigation efforts should be focused when preparing either a HIT or a future full-scale HT-ATES operation.

Heat injection test

Field test sites offer the unique opportunity to collect data and test both characterization and monitoring methods on the scale relevant to later applications. The "TestUM" field test site (www.testum-aquifer.de) was thus set up and is operated to investigate processes induced by heat or mass storage as well as the subsequent environmental impacts using a shallow quaternary glaciogenic aquifer, as e.g., described in Peter et al. (2012a, b) for a CO_2 injection test. Recently, Heldt et al. (2021a) reported the thermal effects, Lüders et al. (2021) geochemical and Keller et al. (2021) biological impacts of a HT-HIT with ≈75 °C injection temperature. The field site construction and the HIT used in this work were carried out by Kiel University and the Helmholtz Centre for Environmental Research (UFZ) within the "TestUM-Aquifer" project, aimed at investigating the induced effects of HT-ATES as well as hydrogen or methane leakage from gas storage sites or transportation infrastructure (Hu et al. 2023). The most relevant geological and technical information about the field site and the HIT are presented in the

following, a more detailed presentation is given in Heldt et al. (2021a, b), who numerically simulated the HIT and Lüders et al. (2021), who investigated the predictability of initial hydrogeochemical effects due to the temperature variations induced by the HIT. They found a good correspondence in predicting temperature-induced maximum concentration changes of environmentally relevant ancillary components by transferring batch test results to the field site, and additionally observed that geochemical conditions approached the initial state after the test.

The "TestUM" field site is located near the town of Wittstock/Dosse, which is about 100 km north of Berlin in Brandenburg, northern Germany (Fig. 1c). It is on a former military airfield and measures about 50 m × 40 m, with a maximum difference in ground elevation of 0.45 m. The shallow geology is of glaciogenic origin and can be simplified vertically by an unsaturated zone (ground level to 3 m below ground level), an upper aquitard (3–6 m), an aquifer (6–15 m) and a lower aquitard (15–20 m). All depth information in this article is reported in meters below ground level. The measured groundwater heads are at approximately 3.3 m depth within the upper aquitard, showing that the groundwater is confined. Natural groundwater flow is approximately from east-northeast to west-southwest, with a mean hydraulic gradient of 0.0011 m/m and a flow velocity of approximately 0.07 m/d.

The experimental setup consists of an injection well and an extraction well, both two-inch wells screened in the aquifer from 7 to 14 m, as well as 17 monitoring wells for temperature measurements (Fig. 1), which were constructed by UFZ Helmholtz Centre for Environmental Research in Leipzig using sonic drilling technology. The extraction well is 40 m upstream from the injection well. Some of the monitoring wells are located in a similar distance to the injection well (Fig. 1a), resulting in three monitoring well groups termed "Circle Inside" (CI, with a distance of 1.2 m to the injection well), "Circle Middle" (CM, 3.1 m distance) and "Circle Outside" (CO, 6.5 m distance), also indicated in Fig. 1.

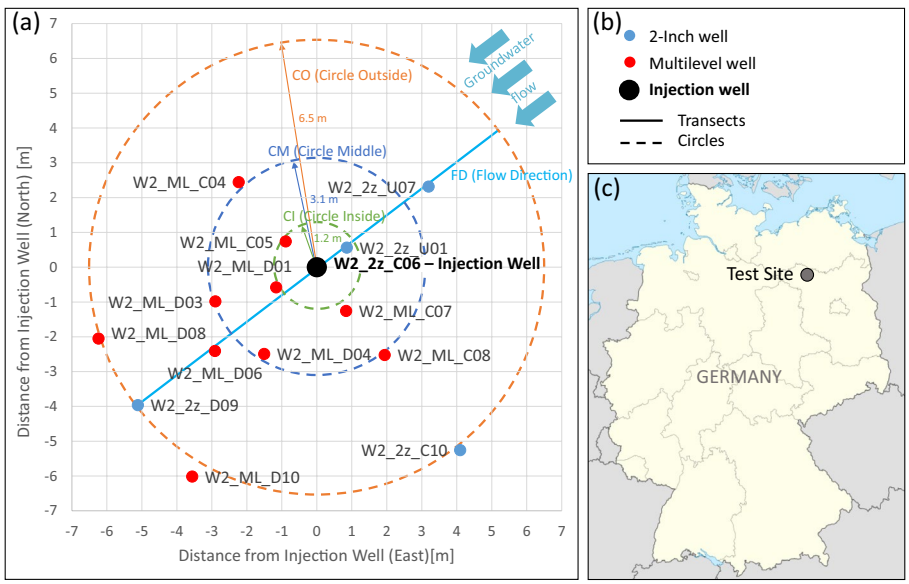

Fig. 1 Overview over the test site with **a** the monitoring wells near the injection well, **b** legend and **c** location of the test site in North Germany (adapted from Heldt et al. 2021a)

The injection well and the temperature monitoring wells are equipped with thermocouple sensors (Type T; Labfacility Ltd., Bognor Regis, United Kingdom and Type T, Class 1; OMEGA Engineering GmbH, Deckenpfronn, Germany; with a resolution of 1 °C), which are installed at the exterior of the wells at the depths of 1 m, 2 m, 4 m, 5 m, 6.5 m, 7.5 m, 9 m, 10.5 m, 13.5 m and 16.5 m.

The injection temperature and the injection flow rate were measured continuously at the well head of the injection well during the HIT. The experiment started at 7:20 pm on 23rd May 2019 and was preliminarily stopped at 5:42 am on 28th May due to a decline in achievable injection flow rate. An attempt to reactivate the injection well from 2:37 pm to 6:43 pm on 29th May resulted in a minor injection of heat, representing 3.13% of the total injected heat. In total, 6437 kWh of heat and 85.74 m^3 of water were injected during 110.47 h of injection. The average injection temperature was 73.76 °C and the average injection flow rate was 12.93 l/min. All data used here are open data and available through Heldt et al. (2021b).

Methods

The sensitivity of the subsurface spatio-temporal temperature distribution on hydraulic and thermal parameters as well as the uncertainty reduction achievable by using both field measurements and model calibration to measured data are investigated using a three-step approach: first, an improved understanding of the heat transport processes initiated by the heat injection test is obtained through a systematic sensitivity analysis by comparing measured and simulated temperature breakthrough curves. In the second step, the model fit to measured temperatures from the field site is evaluated for the parameter ranges derived from general literature values as well as from field investigations, to identify those parameters for which the field-site investigation could reduce the uncertainty most. The third step is performed to investigate, which parameter ranges and thus resulting model uncertainties can be further reduced by calibrating the model to the measured field temperatures.

Model setup

The coupled thermo-hydraulic processes induced by the HIT were simulated in 3D using the open-source finite element code OpenGeoSys (OGS; Kolditz et al. 2012; Kolditz and Bauer 2004). An iterative coupling scheme was applied (Boockmeyer and Bauer 2014; Wang and Bauer 2016) for solving the groundwater flow and heat transport equations in order to consider the effect of temperature-dependent density and viscosity. An automatic time stepping scheme was applied, where the maximum time step size was limited to 60 min and 5 min during the first and second injection phase, respectively. The time steps were chosen smaller for the second injection phase because of the high variability of the injection flow rate. The maximum allowed time step gradually increased from 6 h to 10 days after the end of injection.

The model domain was 300 m × 150 m × 20 m, with the model top representing the ground surface and vertically consisting of the four layers described in "Heat injection test" section. The longer axis of the model domain was aligned parallel to the groundwater flow direction. The finite element mesh consisted of 195,129 nodes and was refined where the steepest pressure and temperature gradients were expected. The horizontal

element size increased from 1.5 cm at the injection well to 15 m at the model boundary and the vertical element size was 0.125–0.25 m.

Governing equations

The governing equations describing the relevant processes implemented in OGS are presented in the following. The groundwater flow equation in a pressure-based formulation for a fully saturated porous medium is (Bear and Bachmat 1990):

$$S\frac{\partial p_W}{\partial t} - \nabla\left(\frac{\mathbf{K}}{\mu_W(T)}\left(\nabla p_W + \rho_W(T)\,g\right)\right) = Q_W, \tag{1}$$

where S [1/Pa] is specific storativity, p_w [Pa] water pressure, t [s] time, $\rho_w(T)$ [kg/m^3] the temperature-dependent water density, T [K] temperature, $\mu_w(T)$ [Pa*s] temperature-dependent dynamic viscosity of water, $\mathbf{K}$ [m^2] the intrinsic permeability tensor, g [m/s^2] the vector of gravitational acceleration and Q_w [1/s] the water source/sink term. As water density $\rho_w(T)$ decreases for higher temperatures in the temperature range of 9–78 °C considered here (Physikalisch-Technische Bundesanstalt 1994), warmer water tends to flow upwards due to buoyancy-driven flow (Collignon et al. 2020; Molz et al. 1983), which results in convection cells. Also, $\mu_w(T)$ is smaller for higher temperatures (Yaws 1995), resulting in a reduced resistance to groundwater flow and thus a reduced pressure gradient due to the hot water injection. Permeability $\mathbf{K}$ is assumed anisotropic in z-direction, with anisotropy described by the anisotropy factor, i.e., the ratio of horizontal to vertical permeability K^h/K^v [-]. S is given by Bear and Bachmat (1990):

$$S = \frac{S_0}{\rho_W(10\,°C)\,g} = \alpha + n\beta, \tag{2}$$

where S_0 [$1/m$] is specific storage, α [1/Pa] is the coefficient of aquifer compressibility, n [-] the porosity and β [1/Pa] the water compressibility.

The heat transport equation includes advective and conductive–dispersive heat transfer processes (Bear and Bachmat 1990):

$$c\rho\,(T)\,\frac{\partial T}{\partial t} + \nabla\,(nc_W\rho_W(T)\,vT) - \nabla(D_H\,\nabla T) = Q_T, \tag{3}$$

where c and c_w [J/kg/K] are the specific heat capacities of the porous medium and of water, respectively. $\rho(T)$ [kg/m^3] is the temperature-dependent density of the porous medium, thus the volumetric heat capacities of the porous medium $c\rho(T)$ [J/m^3/K] and of the water phase $c_w\rho_w(T)$ [J/m^3/K] are considered temperature-dependent as well. v [m/s] is the water flow velocity vector, D_H [W/m/K] the heat conduction–dispersion tensor, and Q_T [J/m^3/s] is the heat source/sink term.

The volumetric heat capacity of the porous medium $c\rho$ [J/m^3/K] is calculated in OGS as:

$$c\rho\,(T) = nc_W\rho_W\,(T) + (1-n)c_S\rho_S, \tag{4}$$

where c_s [J/kg/K] is the specific heat capacity and ρ_s [kg/m^3] is the density of the solid phase, respectively.

The thermal conductivity of the porous medium λ [W/m/K] is given by:

$$\lambda = n\lambda_W + (1 - n)\,\lambda_S, \tag{5}$$

where λ_w and λ_s [W/m/K] are the thermal conductivities of the water and the solid phase, assumed isotropic here. The heat conduction–dispersion tensor in Eq. 3 is given by:

$$D_{H,i,j} = \lambda\delta_{ij} + nc_W\rho_W\left(\beta_t|v|\delta_{ij} + (\beta_1 - \beta_t)\frac{v_i\,v_j}{|v|}\right), \tag{6}$$

where β_l and β_t [m] are the longitudinal and the transversal thermal dispersivity, respectively, v_i and v_j [m/s] are the i and j components of the fluid velocity (with i,j = {x,y,z}) and δ_{ij} [-] is the Kronecker Delta, which is $\delta_{ij} = 1$ for $i = j$ and $\delta_{ij} = 0$ for i ǂ j.

Initial conditions and boundary conditions

The initial temperature distribution in the model was a measured temperature profile. The initial pressure distribution was derived from a spin-up simulation, which accounted for the natural groundwater flow, assigned via Neumann boundary conditions, and for temperature-dependent water density.

No flow temperature boundary conditions were assigned to the lateral model boundaries. Thus, the water was given the temperature of the water present in the aquifer at the inflow boundary and heat loss was allowed by advection only at the outflow boundary. A constant temperature corresponding to the initial condition was assigned at the model bottom, while the transient measured air temperature was assigned to the model top. Pressure distributions derived from the spin-up simulation were assigned as Dirichlet boundary conditions at the lateral model boundaries and no flow boundary conditions were assigned at the model top and bottom.

The injection and extraction wells were simulated by assigning the measured transient flow rates via Neumann boundary conditions to the nodes at the respective well positions. The injected water at the injection well was given the transient measured injection temperature via a Dirichlet boundary condition.

Model parameterization

The numerical model was parameterized based on the field site investigation preceding the HIT. For details on the applied investigation methods and the resulting model fit see Heldt et al. (2021a, b). Table 1 shows the parameter values applied in the base case and in the sensitivity runs. Figure 2 compares the parameter ranges from the literature with the ranges from the site investigation and from the model fit.

For horizontal hydraulic conductivity k_f^h the DIN18130-1 (Hölting and Coldewey 2013) provides order of magnitude estimates of 10^{-5}–10^{-3} m/s for fine to coarse sand, while Domenico and Schwartz (1990) state a range of $2{\cdot}10^{-7}$–$6{\cdot}10^{-3}$ m/s. Using the lower limit of $1{\cdot}10^{-5}$ m/s from DIN18130-1, the literature range for k_f^h was defined here as $1{\cdot}10^{-5}$–$6{\cdot}10^{-3}$ m/s. Measured values of k_f^h for the field site were derived from multilevel pumping tests, which were performed by pumping from one of the three well screens and recording the resulting pressure signals at all three well screens at the observation wells (Linwei Hu, personal communications). k_f^h was obtained by fitting the corresponding analytical solutions (Dougherty and Babu 1984) to each

Table 1 Parameters of the base case and the sensitivity scenarios

	k_f^h m/s	k_f^v m/s	S_0 1/m	λ W/(m·K)	c·ρ MJ/(m³·K)	v_a m/d	n –	β_l m	β_t m
Tested parameter range	*1.00·10⁻⁵*	*1.00·10⁻⁶*	*1.10·10⁻⁵*	*2.00*	**1.94**	*0.008*	***0.34***	*0.001*	*0.001*
	3.00·10⁻⁵	*3.95·10⁻⁶*	***1.26·10⁻⁵***	*2.17*	***2.20***	*0.014*			
	6.60·10⁻⁵	*1.33·10⁻⁵*	***3.39·10⁻⁵***	*2.35*	***2.47***	*0.024*			
	1.45·10⁻⁴	*3.71·10⁻⁵*	***8.62·10⁻⁵***	***2.55***	***2.70***	*0.036*			
	3.19·10⁻⁴	***7.04·10⁻⁵***	*2.19·10⁻⁴*	***2.77***	***2.80***	***0.050***			
	4.78·10⁻⁴	***9.69·10⁻⁵***	*9.80·10⁻⁴*	***3.00***	**2.97**	***0.059***			
	7.15·10⁻⁴	***1.33·10⁻⁴***		**3.19**	**3.26**	***0.070***			
	1.60·10⁻³	***2.24·10⁻⁴***		**3.40**		***0.079***			
	6.00·10⁻³	***4.19·10⁻⁴***				***0.090***			
		7.44·10⁻⁴				*0.116*			
		1.00·10⁻³				*0.175*			
		1.32·10⁻³				*0.274*			
		2.00·10⁻³							

Each parameter was varied independently, the rows of the table are thus not to be understood as connected scenarios

Underlined = base case; **bold** = values within field measurement range; *italic* = within literature range

k_f^h horizontal hydraulic conductivity, k_f^v vertical hydraulic conductivity, S_0 specific storage, λ thermal conductivity, $c{\cdot}\rho$ volumetric heat capacity, v_a groundwater flow velocity, n porosity, β_l longitudinal thermal dispersivity, β_t transversal thermal dispersivity

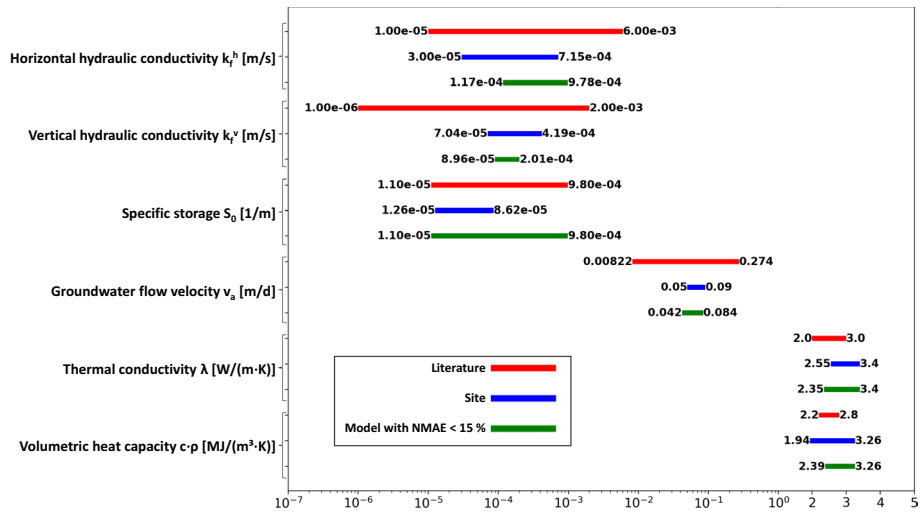

Fig. 2 Parameter ranges derived from the literature (red), the site investigation (blue) and the simulation model (green) using a Normalized Mean Average Error (NMAE, described in Eq. 7) of less than 15% as a measure of model fit

drawdown curve separately. Additional estimates of k_f^h were obtained by sieving, elutriation and slug testing (Heldt et al. 2021a). The resulting range of $3{\cdot}10^{-5}$–$7.15{\cdot}10^{-4}$ m/s for k_f^h is relatively large, reflecting the high variability of k_f^h at this field site, but is still narrower than the literature range of $1{\cdot}10^{-5}$–$6{\cdot}10^{-3}$ m/s. Bloemendal and Hartog (2018) report a k_f^h range of $5.79{\cdot}10^{-5}$–$5.21{\cdot}10^{-4}$ m/s for 204 LT-ATES sites in the Netherlands, which is slightly narrower than the range estimated at the field site. The mean value of k_f^h from the pumping test evaluation of $3.19{\cdot}10^{-4}$ m/s was used for the base case.

The vertical hydraulic conductivity k_f^v literature range is $1{\cdot}10^{-6}$–$2{\cdot}10^{-3}$ m/s. The minimum is based on the minimum value of k_f^h and an anisotropy factor of 10, as often suggested in literature (Hölting and Coldewey 2013; Todd 1980). The maximum is based on the k_f^h maximum and an anisotropy factor of 3, also common in literature (Hölting and Coldewey 2013). Estimates of k_f^v at the field site were obtained by evaluating the multilevel pumping tests by simultaneously fitting all three drawdown curves at one observation well. The values thus obtained span a range of $7.04{\cdot}10^{-5}$–$4.19{\cdot}10^{-4}$ m/s, with a mean of $1.33{\cdot}10^{-4}$ m/s, which was taken as the value of the base case. The measured k_f^v range for the field site is thus significantly smaller than the literature range. Hydraulic conductivity is used throughout this manuscript in text and figures for better comparison to literature values. As shown in Eq. 1, however, hydraulic permeability is required as an input parameter for the non-isothermal groundwater flow equation. The reported hydraulic conductivities are therefore converted to permeabilities for the model runs using ρ_w(10 °C) and μ_w(10 °C).

Literature values for specific storage S_0 were derived from the range in the compressibility of porous media α of $1{\cdot}10^{-9}$–$1{\cdot}10^{-7}$ 1/Pa, the water compressibility β of $4.4{\cdot}10^{-10}$ 1/Pa (Freeze and Cherry 1979) and Eq. 2. The resulting range of S_0 is $1.10{\cdot}10^{-5}$–$9.80{\cdot}10^{-4}$ 1/m. Measured values of S_0 could also be obtained from the pumping tests, together with k_f^h, and exhibit a range of $1.26{\cdot}10^{-5}$–$8.62{\cdot}10^{-5}$ 1/m and are thus within the lower part of the literature range. The base case was parameterized with the mean of $3.39{\cdot}10^{-5}$ 1/m as obtained from the pumping tests (Dahmke et al. 2021).

Literature ranges of thermal conductivity λ and volumetric heat capacity c·ρ are given by Verein Deutscher Ingenieure (2010) and were measured using a KD2 Pro Thermal Properties Analyzer (Decagon Devices Inc., Pullman, USA) on water-saturated sediment liners. The literature range of λ is 2.00–3.00 W/(m·K) and the measured range 2.55–3.40 W/(m·K) with 3.00 W/(m·K) as a representative value parameterizing the base case. Thus, higher values of λ were measured than those from Verein Deutscher Ingenieure (2010). However, Otto (2012) also reports values of up to 3.40 W/(m·K) for sands in a literature summary, thus the measured values of λ can be deemed plausible and indicates the importance of site-specific parameter investigations. The literature range of c·ρ is 2.20–2.80 MJ/(m^3·K) and the measured range 1.94–3.26 MJ/(m^3·K) with a mean of 2.70 MJ/(m^3·K) parameterizing the base case. The larger measured range compared to the range given in the literature could be explained by the applied measuring technique, which is based on a needle giving a temperature pulse to the sediment and another needle recording the resulting temperature development. The distance between these two needles is 6 mm (Decagon Devices 2011), thus the measurements represent a rather small probe volume.

The literature range of 0.008–0.274 m/d for groundwater flow velocity v_a [m/d] is given by Bloemendal and Hartog (2018) for 204 ATES systems in the Netherlands, which have similar hydrogeological conditions than North Germany, and represent plausible hydrogeological conditions for ATES applications. At the field site v_a was estimated based on hydraulic head measurements and from a tracer test, which was carried out during an earlier field campaign (Peter et al. 2012a, b). A range of 0.05–0.09 m/d was derived from these investigations and the base case was parameterized

with 0.07 m/d as the mean value. This range is significantly narrower than the literature range and thus shows the importance of site-specific estimation of v_a.

Porosity n was estimated from dry density and water saturated density measurements of sediment probes and was parameterized as 0.34. Because a variation of n would affect mainly the thermal parameters, which are varied independently as described above, a systematic variation is not included here. Additionally, the change in v_a due to a porosity change is fully compensated by the thermal retardation, so that heat transport is insensitive to this variation. The longitudinal and the transversal thermal dispersivity β_l and β_t were chosen as 0.001 m, which proved to be small enough to make the thermal behavior insensitive to this parameter based on temperature breakthrough curve comparison. β_l and β_t were therefore excluded from the sensitivity analysis.

Results

Figure 3 compares measured and simulated temperature breakthrough curves for the base case and the scenarios with varied k_f^v, as listed in Table 1. The measured temperatures show a fast increase at a distance of 1.2 m to the injection well, due to the hot water injection and the induced fast advective heat transport. The temperature rises above 60 °C at all three depths during the injection and decreases after the hot water injection

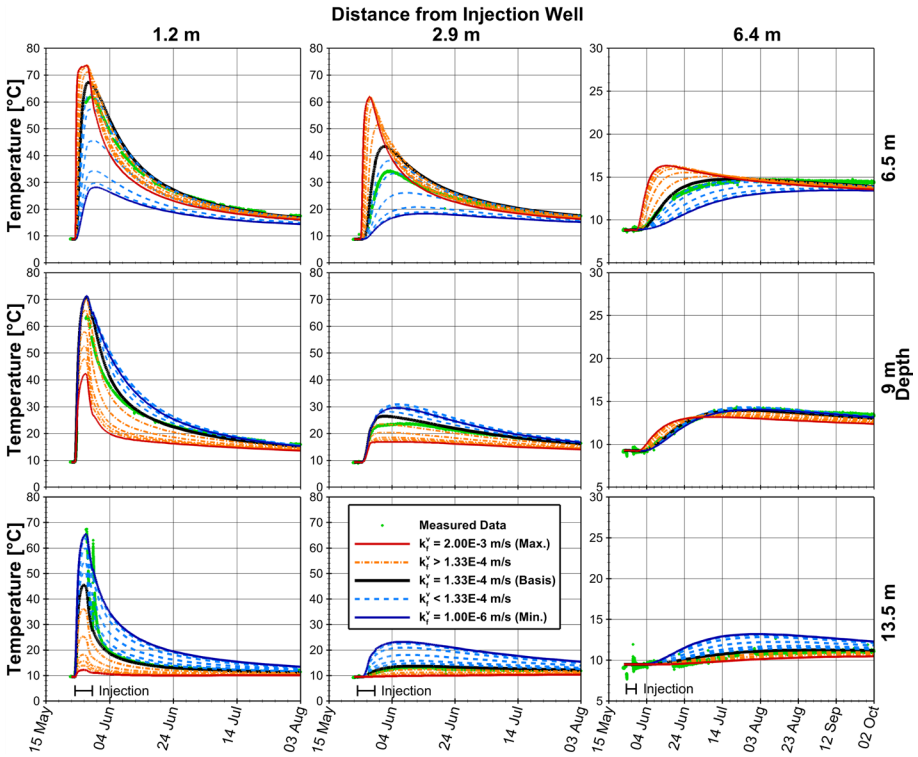

Fig. 3 Measured (green) and simulated temperature breakthrough curves for the base case (black) and smaller (light blue/dark blue) as well as larger (orange/red) values of vertical hydraulic conductivity k_f^v, shown for different depths and distances to the injection well. The maximum and minimum scenarios, as derived from the literature, are displayed as the solid red and solid blue lines, respectively, while the remaining sensitivity scenarios are displayed as dashed or dash-dotted lines. The data in 6.4 m and in 2.9 m distance from the injection well are from wells W2_2z_D09 and W2_ML_D04, respectively. The data in 1.2 m distance are from W2_ML_C05 in 6.5 m and 9 m depth and from W2_2z_U01 in 13.5 m depth, due to temperature sensor failure. Temperature as well as time axis are rescaled for the right-hand side column

stopped. Temperatures decrease faster at the lower depth of 13.5 m compared to the shallower depths, which is likely caused by induced convection (Heldt et al. 2021a). At the intermediate distance of 2.9 m, temperature peaks are less pronounced and do not exceed 40 °C, which is due to a larger fraction of conductive heat transport here. For the same reason, the temperature increase is slower and the peak is later at 6.4 m distance, where temperatures do not exceed 15 °C. Due to the mainly radially decreasing temperature distribution induced and the smaller temperature gradients at larger distances, temperatures do not decrease significantly during the time interval displayed. Also, for larger radial distances, temperatures are higher in the upper part of the aquifer, which can be attributed to buoyancy-driven flow of the injected hot water.

As can be also seen from Fig. 3, the simulated base case shows a relatively good overall agreement with the measured temperatures.

Because the intensity of induced buoyancy flow is sensitive on k_f^v, model results using a higher k_f^v show the effects of more intense convection. This can be seen in Fig. 3, where the scenarios with higher k_f^v show higher maximum temperatures at the depth of 6.5 m compared to the base case. For example, the temperature maximum at 6.5 m depth in 2.9 m distance from the injection well increases from 43 °C in the base case to 62 °C in the scenario with the highest k_f^v. At the lower depth of 9 and 13.5 m a higher k_f^v results in lower peak temperatures, which indicates upward movement of heat with increasing k_f^v due to thermal convection. The higher temperatures at the aquifer top also result in an increased heat loss to the upper confining layer, resulting in a faster temperature decrease there. A higher k_f^v leads to earlier peak times at all locations due to increased convection. A reduction of k_f^v reduces the effects of induced convection as well, which leads to a more equal temperature distribution with depth, as the upward flow of hot water is reduced, as well as to later peak times (see Fig. 3).

The effect of k_f^v on buoyancy flow can also be seen in Fig. 4, which shows the simulated temperature distribution at a representative time using a vertical as well as a horizontal cross section for values of k_f^v corresponding to the base case, as well as the literature-based and measured minima and maxima. Based on the lowest k_f^v, Fig. 4e shows a heat plume which is vertically symmetric around its center in the middle of the aquifer and thus does not show any influence from thermal convection. With increasing k_f^v (Fig. 4d-a), thermal convection is increased and thus the heat plume moves more and more towards the top of the aquifer while the heat plume shape becomes gradually distorted. This also results in lower maximum temperatures, as the volume to surface ratio of the heat plume decreases with increasing k_f^v and more heat is conductively transferred to the upper aquitard. The horizontal cross-sections show, that the horizontal extent of the heat plume increases with increasing k_f^v. For example, the diameter of the 15 °C isoline increases by 65% from 6.5 m using $k_f^v = 1.00 \cdot 10^{-6}$ m/s (Fig. 4e) to 10.7 m using $k_f^v = 2.00 \cdot 10^{-3}$ m/s (Fig. 4a). As the cross section is within the upper part of the aquifer, this also indicates that more heat rises to the top of the aquifer as k_f^v increases. The highest temperature in the center of the horizontal cross-sections, however, is simulated using $k_f^v = 7.04 \cdot 10^{-5}$ m/s (Fig. 4d), as in this scenario the vertical heat plume center is closest to the cross-section depth of 7.5 m.

In analogy to Fig. 3, Fig. 5 shows the comparison of the scenarios with different λ to the measured temperature breakthrough curves. The temperature changes are higher in

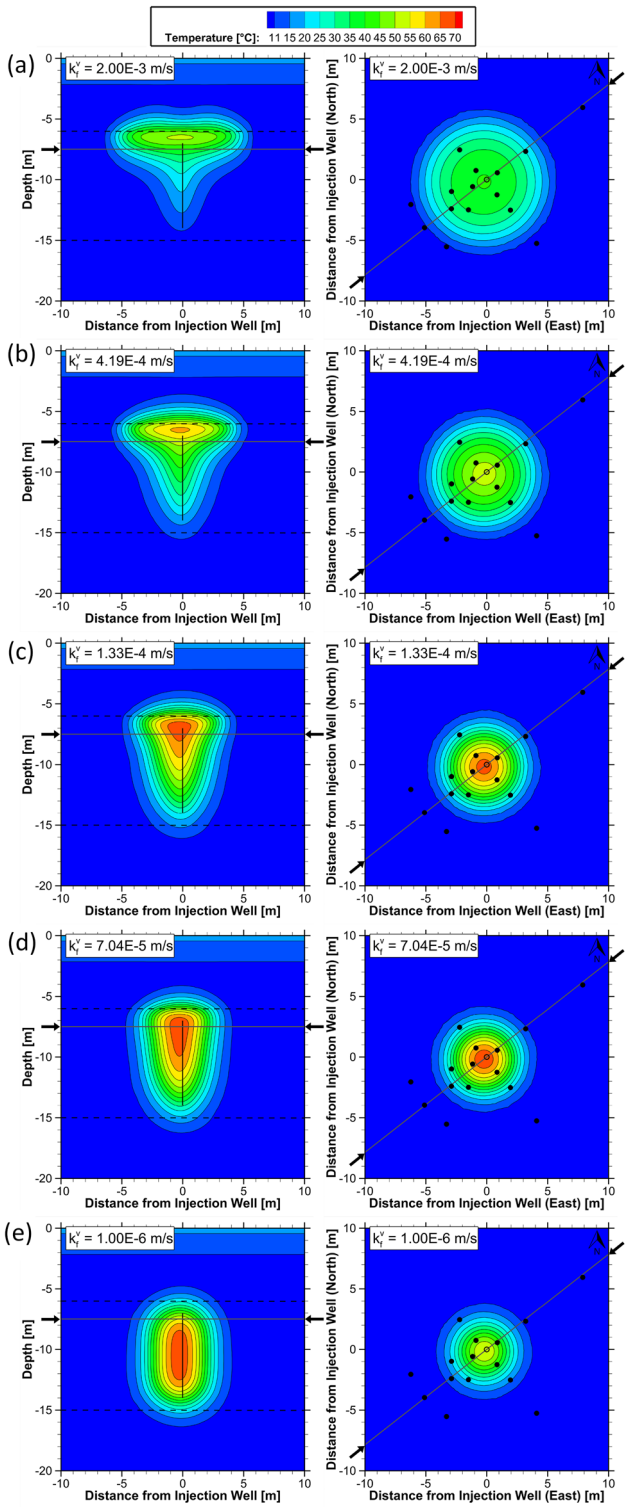

Fig. 4 Simulated heat plume 2 days after the hot water injection has stopped (31st of May at 7 pm) for different values of vertical hydraulic conductivity k_f^v. The k_f^v value of **a** corresponds to the maximum from literature, **b** to the measured maximum, **c** is the base case, **d** is the measured minimum and **e** the literature minimum. The left-hand side figures show a vertical transect through the injection well along the groundwater flow direction, which is also marked in the right-hand side figures, which show a horizontal cross section in top view at 7.5 m depth

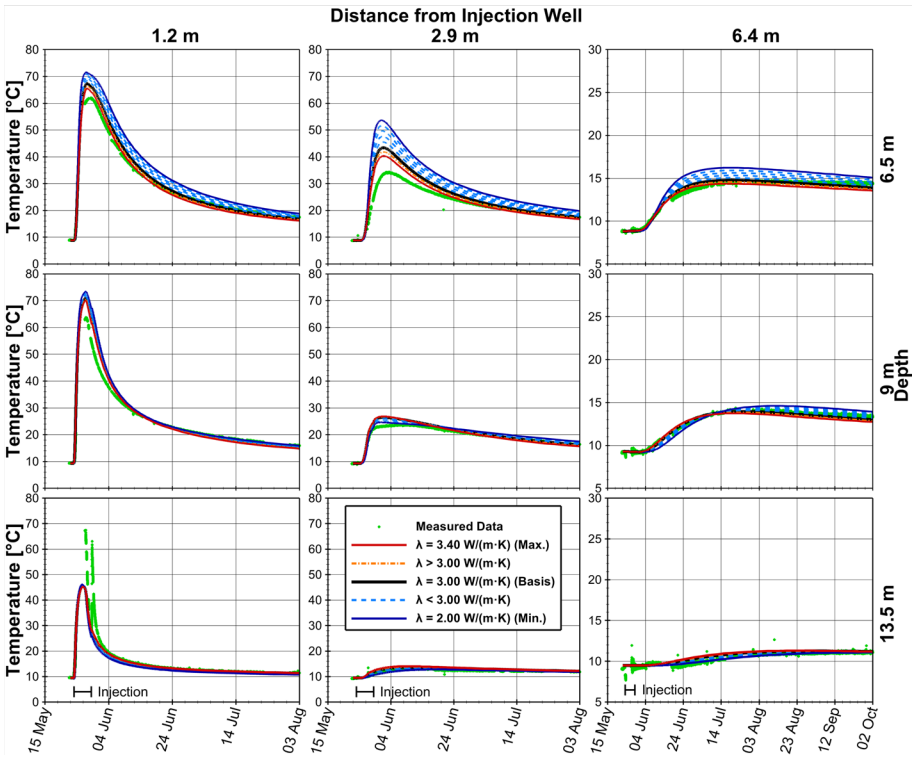

Fig. 5 Measured (green) and simulated temperature breakthrough curves for varied thermal conductivity λ, shown for different depths and distances to the injection well. Measured temperatures are obtained from the same wells as in Fig. 3, temperature as well as time axis are rescaled for the right-hand side column. The black line indicates the base case, the blue lines indicate the scenarios with decreased λ and the orange/red lines indicate the scenarios with increased λ. The maximum and minimum scenarios, as derived from the literature, are displayed as the solid red and solid blue line, respectively, while the remaining sensitivity scenarios are displayed as dashed or dash-dotted lines

the scenarios with decreased λ than in those with increased λ, which is mainly due to the larger relative change of λ (from 3 W/(m·K) in the base case to 2 W/(m·K) and 3.40 W/(m·K), respectively). A decrease in λ results in higher temperatures at 6.5 m depth and lower temperatures at 13.5 m depth. For example, the peak temperature in 1.2 m distance and 6.5 m depth rises from 67 °C in the base case to 72 °C with the lowest λ. The impact is largest at the distances of 2.9 m and 6.4 m, when considered in relation to the total temperature rise. The increasing heat transfer to the aquifer top with decreasing λ can be explained by the impact of λ on the intensity of buoyancy-driven flow. A reduction of λ reduces the conductive heat transfer in the aquifer in both lateral and vertical direction. Thus, the temperature gradients as well as density gradients are increased, which results in increased buoyancy flow. Furthermore, a lower λ decreases the vertical temperature conduction where a convection-induced temperature gradient is already in place and thus increases the unequal vertical heat distribution. The temperature changes through the variation of λ are less pronounced than these induced by changing k_f^v, thus the thermal behavior is more sensitive to k_f^v than to λ.

The sensitivity of the parameters k_f^h, S_0, $c \cdot \rho$ and v_a is described briefly in the following and the corresponding figures are shown in the appendix. Variation of k_f^h showed that k_f^h affects convective flow by increasing or decreasing the horizontal component of the

induced convection. This results in a stronger upward heat movement for larger k_f^h, as shown in App Fig. 9, which causes stronger tilting and higher temperatures in the upper part of the aquifer. The thermal behavior is found to be more sensitive to k_f^h than to λ, but less sensitive than to k_f^v. The specific storage S_0 does not have any impact on the thermal behavior (App Fig. 10). The reason is that this parameter only determines the short-term temporal evolution of the pressure field due to the hot water injection, but does not affect advective heat transport as the flow velocities are governed by the injection rate.

An increase of c·ρ leads to smaller temperature changes per amount of heat injected and thus reduces the conductive heat flow by reducing thermal diffusivity. This in turn increases the intensity of buoyancy-driven flow, as more pronounced temperature gradients are maintained. This effect is thus analogous to a decrease of λ. Furthermore, an increase of c·ρ increases thermal retardation, thus reducing advective heat transport away from the injection well and shifting the temperature peaks to later times and lower temperatures (compare App Fig. 11).v_a influences the advective heat transport with the ambient groundwater flow. An increased v_a thus causes a higher peak temperature and an earlier peak time at the larger distances from the injection well and a faster cooling at all monitoring locations (App Fig. 12). The sensitivity to v_a is pronounced given the large range of applied values (0.008–0.274 m/d), especially at the distance of 6.4 m from the injection well. Here the thermal behavior is more sensitive to v_a than to all other parameters, while at 1.2 m it is less sensitive to v_a than to k_f^v.

In order to describe the sensitivity of the thermal behavior on the investigated parameters in a quantitative manner and to be able to assess the agreement between the measured and the simulated temperatures, the Normalized Mean Average Error (NMAE) is used here (Janssen and Heuberger 1995):

$$\mathrm{NMAE} = \frac{\sum_{i=1}^{N} |P_i - O_i|}{N\,\overline{O}}. \tag{7}$$

Here P are simulated (predicted) and O are measured (observed) temperatures at each measurement location, respectively. N is the number of observations and $\overline{O}$ is the mean of all measured temperature differences relative to the initial measured temperature at one location. The NMAE thus represents the average mismatch between the simulated and measured temperatures relative to the average measured temperature increase of each breakthrough curve. Thus, a NMAE of zero describes a perfect model fit, increasing for worse model fits with no upper limit. Temperature measurements from 4 m down to 13.5 m depth at all observation wells within 6.6 m distance to the injection well were used for model fit evaluation. The NMAE was calculated for each measurement location separately and then averaged over all measurement locations. The NMAE is commonly used in e.g., hydrology or agricultural sciences to evaluate model quality (Nendel et al. 2011; Rakhshandehroo et al. 2018) and was applied successfully by Heldt et al. (2021a, b) to assess the quality of the predictive model of the HIT thermal impacts. Here, the NMAE allows for an integrated measure to assess the impact of parameter variations on the overall model quality.

Figure 6 therefore summarizes the sensitivity of the model quality, as measured by the NMAE, to the thermal and hydraulic parameters varied as described above. Due

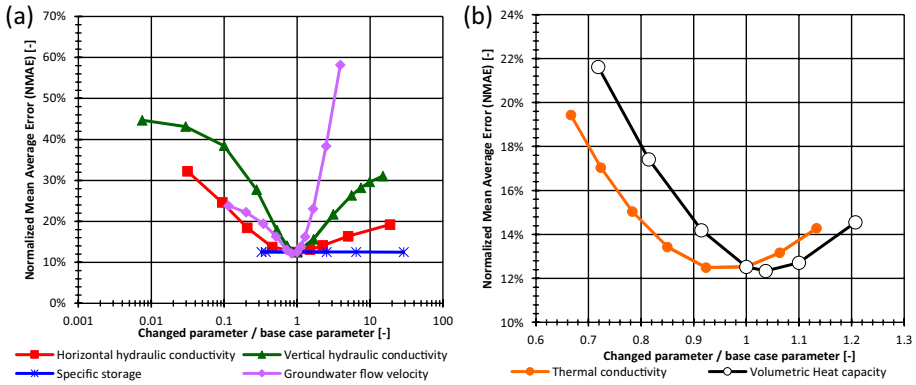

Fig. 6 Sensitivity of the Normalized Mean Average Error (NMAE) calculated from the measured and simulated temperatures to **a** the hydraulic parameters horizontal and vertical hydraulic conductivity k_f^h and k_f^v, specific storage S_0 and groundwater flow velocity v_a and **b** to the thermal parameters thermal conductivity λ and volumetric heat capacity c·ρ. Parameter ranges investigated correspond to the total range of values as given in Table 1

to the large natural variability of the hydraulic parameters k_f^h, k_f^v, S_0 and v_a, these are depicted using a logarithmic axis (Fig. 6a), while the thermal parameters λ and c·ρ (Fig. 6b) are displayed using a linear axis. Figure 6a shows that both an increase and a decrease of k_f^h and k_f^v from the base case result in significantly higher values of the NMAE, representing a worse fit of simulated to measured temperatures. This is plausible also when inspecting Fig. 3 and App Fig. 9, as there the visible discrepancy is increasing for larger parameter variations. Therefore, no reduction of the NMAE is possible by using other values of hydraulic conductivity, which means that the optimal values of k_f^h and k_f^v are already those used in the base case. This finding thus shows that multilevel pumping tests are a suitable method for determining the hydraulic conductivities to parameterize the flow and heat transport model used here, as already found by Heldt et al. (2021a). Comparison of the NMAE values for k_f^h and k_f^v furthermore reveals that the NMAE curve for k_f^v is steeper on both sides of the base case, indicating that the model fit gets worse faster for k_f^v than for k_f^h for the same relative parameter change. The reason is, as discussed above, that the influence of k_f^v on buoyancy flow is stronger than for k_f^h. As this strong sensitivity of the NMAE on the hydraulic conductivities with distinct optimum values shows, these parameters can be determined with good accuracy by inverse modeling.

For variations of the flow velocity v_a, the corresponding NMAE values also have a minimum near the base case. Closer inspection (better visible in Fig. 7) shows that a slightly reduced NMAE of 12.2% is achieved at the lower v_a of 0.059 m/d, with the base case NMAE being 12.5% at a v_a of 0.07 m/d. However, larger variations of v_a result in large values of the NMAE and thus a significantly worse model fit. The increase of the NMAE for higher v_a values is the steepest of all parameters varied, with the highest v_a of 0.274 m/d resulting in the highest observed NMAE of 58.2%, while for lower v_a the increase of the NMAE is less distinct. The sensitivity of NMAE to v_a is thus in effect similar to that of k_f^v and also indicates, that the flow velocity can be clearly obtained from inverse modeling and fitting the model to the data.

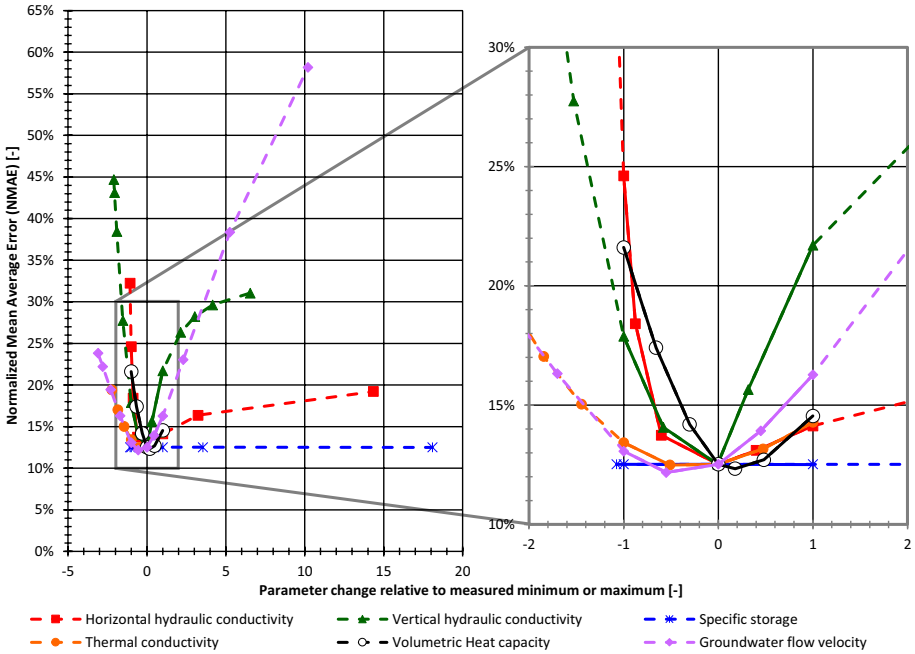

Fig. 7 Sensitivity of the Normalized Mean Average Error (NMAE) to parameter variation, which are normalized to the range of field measurements. Thus, -1 corresponds to the minimum and 1 to the maximum measured values, respectively, while 0 represents the base case. 2 on the x-axis consequently means a value corresponding to the base case plus twice the difference to the maximum measured value. Solid lines represent parameter ranges estimated at the field site and dashed lines show the range obtained from the literature. The right-hand side figure is a zoom on the area marked by a grey frame on the left-hand side figure

For the variation of the specific storage S_0, no change of the NMAE is found, which shows that the model results are insensitive to the value of S_0. This parameter can thus not be inferred from model fitting, but also has no discernible effect on resulting temperatures.

Sensitivity of the NMAE to variations of the thermal parameters is shown in Fig. 6b. For both parameters, a similar behavior is found, i.e., a minimum close to the base case and an increase in the NMAE with increasing parameter variation, for both higher and lower values. A maximum NMAE of about 22% is found for the variations of λ and c·ρ, indicating that the NMAE shows smaller changes due to variations of the thermal parameters than to variations of k_f^v, v_a and k_f^h. This is not due to a generally lower sensitivity of those parameters, as is also evident from Fig. 7, but due to the lower natural variability of c·ρ and λ, which do not vary over several orders of magnitude like k_f^h, k_f^v and v_a, and can thus be determined with more confidence from literature or field measurement values. For both the base case (3.00 W/(m·K)) and a slightly reduced λ of 2.77 W/(m·K) the same NMAE is found, indicating that the optimum would be somewhere in between. Regarding c·ρ, the NMAE could be slightly reduced from 12.5% for the base case to 12.3% using a c·ρ of 2.80 MJ/(m^3·K) instead of 2.70 MJ/(m^3·K). Relative changes and maximum NMAEs for both parameters are similar and show an optimum near or at the base case, which shows that also these thermal parameters could be obtained from inverse modeling.

Up to now, the full range for each parameter as given by general literature values was investigated, thus representing the ranges expected without detailed measurements of parameter values from the field site. As shown in Table 1, the parameter range obtained from the field site is smaller than from the literature, except for $c \cdot \rho$. It is expected that local measurements of these parameters obtained from the field site will reduce uncertainty and improve the model fit to the data. Therefore, Fig. 7 distinguishes between the parameter range from site-specific field measurements (using full lines) and the range from general literature (using dashed lines) as well as showing the sensitivity of the NMAE normalized to the range of field measurements. As Fig. 6 shows, a significant reduction in the NMAE can be obtained for most parameters by restricting the parameter range to measured field-site ranges.

For example, the NMAE of the highest literature value of v_a is 58%, but only 16% for the measured maximum v_a of 0.09 m/d, while the NMAE for the minimum measured v_a is 13% compared to 24% for the minimum value from literature. This shows, that the model fit to the measured temperatures could thus be improved significantly by applying a measured v_a range to the model instead of a literature range. Similarly, NMAEs for k_f^v and k_f^h are also significantly reduced. For λ, only the smaller values from the literature range could be ruled out by the site measurement range, while no NMAE reduction is achieved for $c \cdot \rho$, because the field measurement range is wider than the literature range. Since NMAE is insensitive to S_0, the application of a field-site specific range of this parameter did not result in lower NMAE values and is thus irrelevant for HT-ATES thermal behavior. These findings show, that especially for the hydraulic parameters a significant reduction in the model error NMAE and thus a better representation of measured temperatures by the model is obtained, if local field measurements are available and used to restrict the wide literature-based parameter range. This clearly demonstrates the worth of field measurements of these parameters. The improvement of the model fit is less pronounced for the thermal parameters, because the field site range is more similar to the literature range. However, also a distinct improvement of the model fit can be obtained for λ.

As the previous simulations for parameter sensitivity have shown, a clear minimum of the NMAE exists for most parameters. Therefore, the NMAE can be used to further restrict the parameter values of the hydraulic and thermal parameters. This resembles the typical procedure during inverse modeling, where the mismatch between simulated and observed temperatures is used to identify the unknown or uncertain model input values. The numerical simulation model is thus employed as a parameter investigation tool, and a parameter range for k_f^v, k_f^h, v_a, λ and $c \cdot \rho$ for a given value of the NMAE is derived. The parameter ranges are read from Figs. 6 and 7 and given in Fig. 8 for an NMAE of 13%, 15% and 17%.

With NMAE < 15% the range of k_f^v is found to be $8.96 \cdot 10^{-5}$–$2.01 \cdot 10^{-4}$ m/s, which is smaller than the range of $7.04 \cdot 10^{-5}$–$4.19 \cdot 10^{-4}$ m/s derived from the field measurements. The corresponding range of k_f^h is $1.17 \cdot 10^{-4}$–$9.78 \cdot 10^{-4}$ m/s, as compared to $3.00 \cdot 10^{-5}$–$7.15 \cdot 10^{-4}$ m/s from the field measurements. The upper limit of k_f^h using NMAE < 15% is thus actually larger than the field values, however the total k_f^h range is still smaller due to an increased minimum value of k_f^h. Likewise, the maximum v_a decreases from 0.09 m/d to 0.84 m/d and the minimum $c \cdot \rho$ increases from 1.94 MJ/(m^3·K) to 2.40 MJ/(m^3·K),

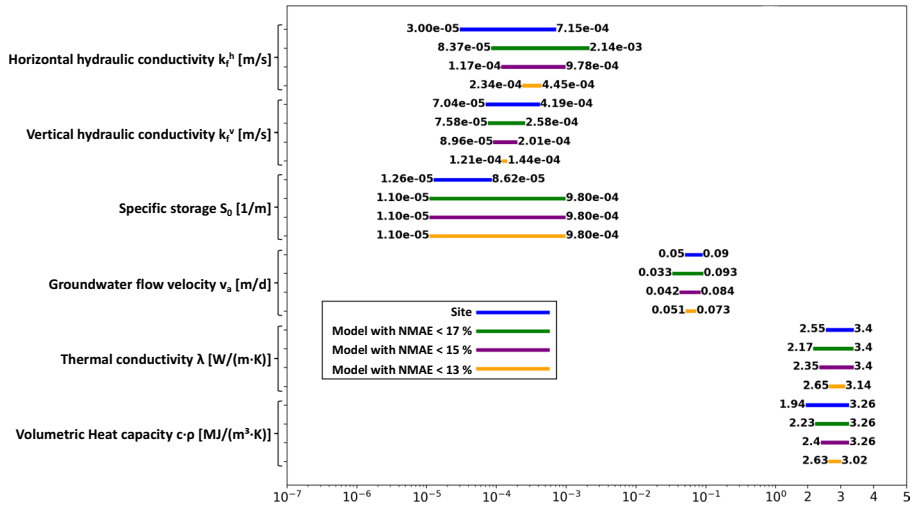

Fig. 8 Parameter ranges derived from the field site measurements and from evaluation of the model fit to the measured temperatures with the Normalized Mean Average Error (NMAE) as a measure of model fit. Ranges are displayed for different fits, corresponding to NMAEs of 17%, 15% and 13%

while the minimum v_a or the maximum c·ρ cannot be further restricted. A range reduction is not possible for λ using a NMAE < 15%. Due to the insensitivity of model results on S_0, no range can be derived based on an improved model fit.

As these results show, using a NMAE of 15% yields narrower ranges for most parameters than field values. However, using an even lower NMAE allows to further constrain the ranges of these parameters and a higher NMAE results in wider parameter ranges. Therefore, parameter ranges are also determined for smaller NMAEs of 13% and higher NMAES of 17% and given in Fig. 8. For example, the range of k_f^v with NMAE < 15% ($8.96 \cdot 10^{-5}$–$2.01 \cdot 10^{-4}$ m/s) reduces to $1.21 \cdot 10^{-4}$–$1.44 \cdot 10^{-4}$ m/s for a NMAE of 13%, but increases to $7.58 \cdot 10^{-5}$–$2.58 \cdot 10^{-4}$ m/s for a NMAE of 17% (see Fig. 8). A further reduction than with a NMAE of 13% is not possible, because no NMAE obtained in the sensitivity simulations reported above (see Figs. 6 and 7) is smaller than 12%. The parameters, of which the ranges could be reduced most are the parameters, the thermal behavior is most sensitive on. These parameters are, in order of decreasing sensitivity, k_f^v, k_f^h, v_a, c·ρ, λ and S_0.

Discussion

The temperature distribution resulting from a heat injection in an aquifer is influenced by a set of hydraulic and thermal parameters. The aim of this work is to identify the parameters, for which the parameter ranges and thus parameter uncertainty can be significantly reduced by using field data as compared to literature data. For those parameters field site measurements are thus recommended prior to a heat injection, in order to obtain reliable predictions of the spatio-temporal temperature distribution. Furthermore, the additional range reduction obtained by calibrating the model to the measured field-site temperatures after a heat injection is evaluated. This identifies the parameters for which an improved estimate can be expected using inverse modeling.

The parameter ranges of both k_f^v and k_f^h could be significantly reduced by applying field measurement ranges and could be further reduced by model calibration. This is due to a pronounced sensitivity of the thermal behavior to hydraulic conductivity, as is evident from the sensitivity analysis also. The wide range of v_a measurements from the literature and the resulting uncertainties could be significantly reduced using field measurements, however no significant further reduction was possible by model calibration. However, it is expected, that a range reduction would have been possible by model calibration, if the measured range would have been wider, since the spatial temperature distribution is sensitive on v_a. The literature range of S_0 could be reduced at the field site, but since S_0 had no impact on the thermal behavior, this did not reduce uncertainties and no range reduction was possible through model fit evaluation. For the thermal parameters λ and $c{\cdot}\rho$, no significant reduction of parameter ranges and the resulting simulation uncertainties were found by using field measurements as compared to literature values. For both parameters, this is due to the field measurement ranges, which are on the order of the literature ranges. $c{\cdot}\rho$ was measured in a wider range than it is common in the literature, so that the pronounced sensitivity to $c{\cdot}\rho$ can thus be seen as an effect of the large measurement range. This surprising finding is probably due to the small sample volume tested in the measurements using the specific measurement device. A spatially integrative method, like a thermal response test, would probably have resulted in narrower parameter ranges and thus a reduced model uncertainty. Accounting for a more integrative method for thermal parameters, this shows that the employed field investigation methods yield significantly improved model predictions as compared to using a literature-based data set. Using inverse calibration after a heat injection test allowed in this case especially a better estimation of the hydraulic parameters.

Because model calibration yielded better model results compared to using parameters from prior investigation, a HIT prior to the implementation of an ATES or especially a HT-ATES operation would help to significantly constrain model predictions. This would improve model parametrization before the operation phase, allowing for improved prediction of thermal impacts and HT-ATES operation characteristics, such as thermal recovery or return flow temperatures. These aspects are crucial for HT-ATES viability and feasibility from both a regulatory as well as operative perspective. Later, during the operational phase of an ATES system, more monitoring data will become available and model predictions can be further improved by model calibration to measured temperatures from the operational phase.

Although the governing processes of HT-ATES and HT-HIT are the same, the HIT in this study differs from a typical HT-ATES application with respect to the operational scheme. For a HT-ATES operation, heat transport is expected to be advection-dominated due to the alternating injection and extraction of water, while heat conduction will more determine the longer-term temperature field and the induced temperature changes on the fringes of the ATES site. Although the current HIT was more conduction-dominated than a cyclic HT-ATES, due to the short injection period and the long monitoring period, the observed thermal behavior is still expected to be representative for parameter estimation. The strong sensitivity of the thermal behavior to k_f^h and k_f^v can be attributed to the induced buoyancy flow, and will be also typical during HT-ATES operation.

In contrast to that, buoyancy flow does not play a major role in low temperature-ATES (LT-ATES) systems. This explains the finding of Bridger and Allen (2014) that the thermal behavior was more sensitive on variations of the hydraulic gradient than on k_f^h, as they examined a LT-ATES system with 14 °C injection temperature. In accordance with the present study, Gao et al. (2019) (injection temperature of 50 °C) and Jeon et al. (2015) (90 °C) identified k_f^h as having the highest impact on the thermal behavior, for which they used the recovery efficiency as a measure. Schout et al. (2014) (90 °C) and Sheldon et al. (2021) (up to 300 °C) found the recovery efficiency of HT-ATES to be most sensitive on k_f^h and k_f^v within the parameters considered. This finding is corroborated for a HT-HIT in this study.

The lowest NMAE of 12.2% and thus best model fit of all evaluated scenarios is close to the NMAE of 12.5% obtained for the base case. This shows, that the model parametrization based on the field measurements is already close to the achievable optimum. The parameters yielding the NMAE optimum are thus expected to be close to the base case parametrization. Therefore, we provided specific parameter ranges corresponding to about the same degree of model fit instead of one optimum parameter set. The NMAE of $\approx$12% is thus the best model fit that can be obtained by varying the parametrization of the used model.

The measured temperature distribution exhibits some influence of spatial heterogeneity, as temperatures measured in the same distance from the injection well and at the same time in some cases showed large differences, which could not be attributed to the influence of ambient groundwater flow (Heldt et al. 2021a). For capturing these spatial effects and improving model accuracy by reducing the remaining mismatches between measured and simulated temperatures, a spatial variability of the hydraulic as well as the thermal parameters would have to be accounted for. However, on the small scale of the heat injection test presented here, the data obtained from the site do not allow for a characterization of this spatial variability, so that a full model fit cannot be achieved.

Conclusions

- The sensitivity analysis of the subsurface spatio-temporal temperature distribution shows a pronounced sensitivity of the thermal behavior to vertical and horizontal hydraulic conductivity as well as groundwater flow velocity, a smaller sensitivity to volumetric heat capacity and thermal conductivity and no sensitivity to specific storage. This is illustrated by the maximum increase of the Normalized Mean Average Error (NMAE) with respect to the base case, which has an NMAE of 12.5%. For groundwater flow velocity, it rises to 58% maximally and for vertical and horizontal hydraulic conductivity to 45% and 32%, respectively, while it remains below 22% for the thermal parameters and no increase is found for specific storage.
- The focus of field investigations for a heat injection test or an aquifer storage operation should thus be on the hydraulic parameters, as this will allow for the largest reduction in prediction uncertainty.
- The sensitivity on the hydraulic and thermal parameters as well as the uncertainty and parameter range reduction achievable by using field measurements and model calibration as compared to literature data indicate that a significant reduction in

model prediction uncertainty can be achieved. Since monitoring data will be gathered during HT-ATES operation, a continued data-driven model improvement is possible and recommended. This is especially valuable for the parameters, which are difficult to measure in the field.

- A heat injection test prior to a HT-ATES operation allows to significantly improve model prediction of the induced temperature effects and the thermal impacts. A suitable monitoring network can be designed using a priori estimated parameters, as they provide a sufficient approximation of the temperature distribution.

Appendix

See Figs. 9, 10, 11, 12.

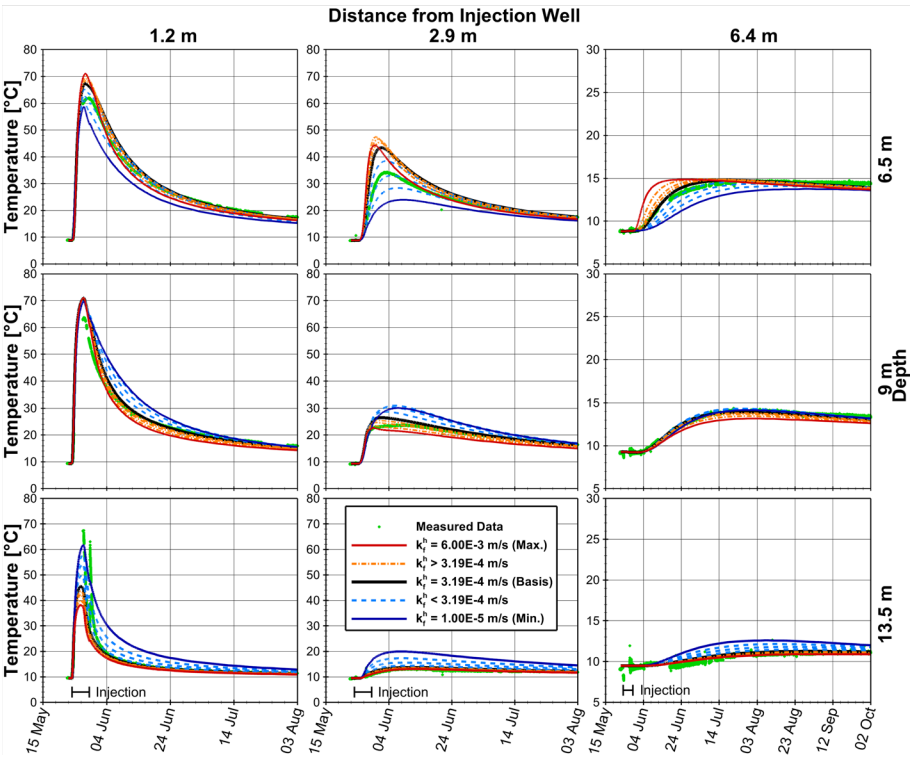

Fig. 9 Measured (green) and simulated temperature breakthrough curves for varied horizontal hydraulic conductivity k_f^h, shown for different depths and distances to the injection well. Measured temperatures are obtained from the same wells as in Fig. 3, temperature as well as time axis are rescaled for the right-hand side column. The black line indicates the base case, the blue lines indicate the scenarios with decreased k_f^h and the orange/red lines indicate the scenarios with increased k_f^h. The maximum and minimum scenarios, as derived from the literature, are displayed as the solid red and solid blue line, respectively, while the remaining sensitivity scenarios are displayed as dashed or dash-dotted lines

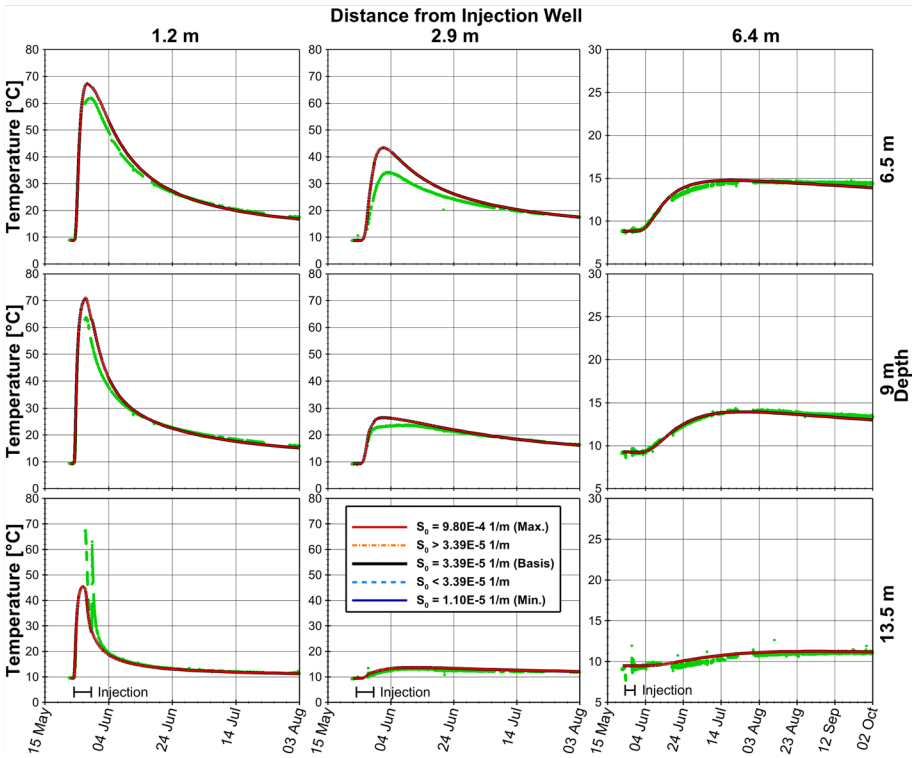

Fig. 10 Measured (green) and simulated temperature breakthrough curves for varied specific storage S_0, shown for different depths and distances to the injection well. Measured temperatures are obtained from the same wells as in Fig. 3, temperature as well as time axis are rescaled for the right-hand side column. The black line indicates the base case, the blue lines indicate the scenarios with decreased S_0 and the orange/red lines indicate the scenarios with increased S_0. The maximum and minimum scenarios, as derived from the literature, are displayed as the solid red and solid blue line, respectively, while the remaining sensitivity scenarios are displayed as dashed or dash-dotted lines

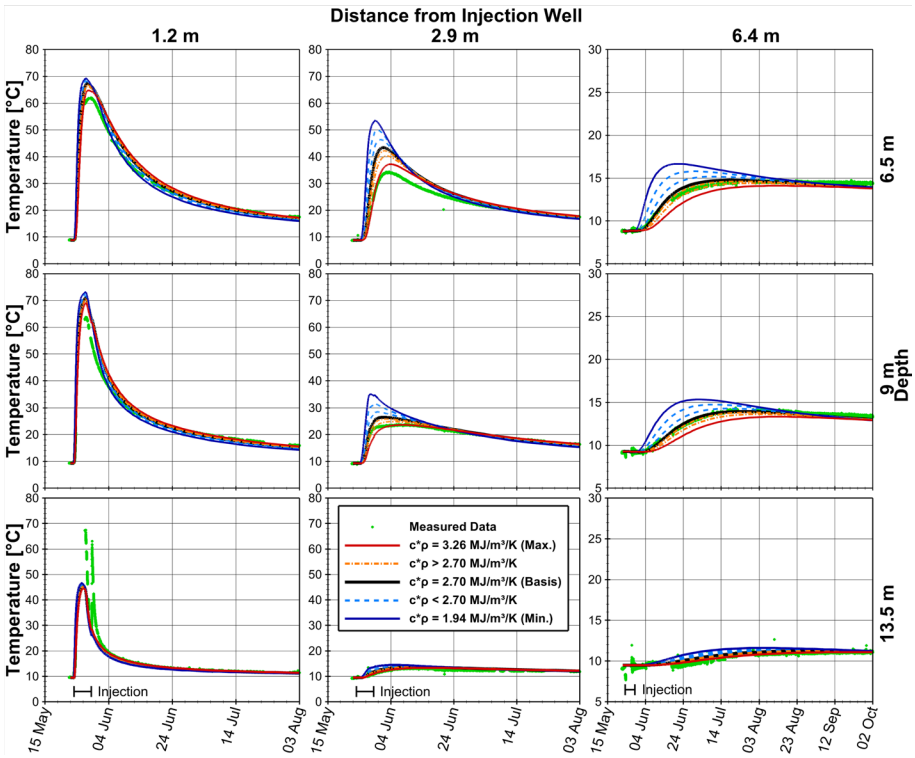

Fig. 11 Measured (green) and simulated temperature breakthrough curves for varied volumetric heat capacity c·ρ, shown for different depths and distances to the injection well. Measured temperatures are obtained from the same wells as in Fig. 3, temperature as well as time axis are rescaled for the right-hand side column. The black line indicates the base case, the blue lines indicate the scenarios with decreased c·ρ and the orange/red lines indicate the scenarios with increased c·ρ. The maximum and minimum scenarios, as derived from the literature, are displayed as the solid red and solid blue line, respectively, while the remaining sensitivity scenarios are displayed as dashed or dash-dotted lines

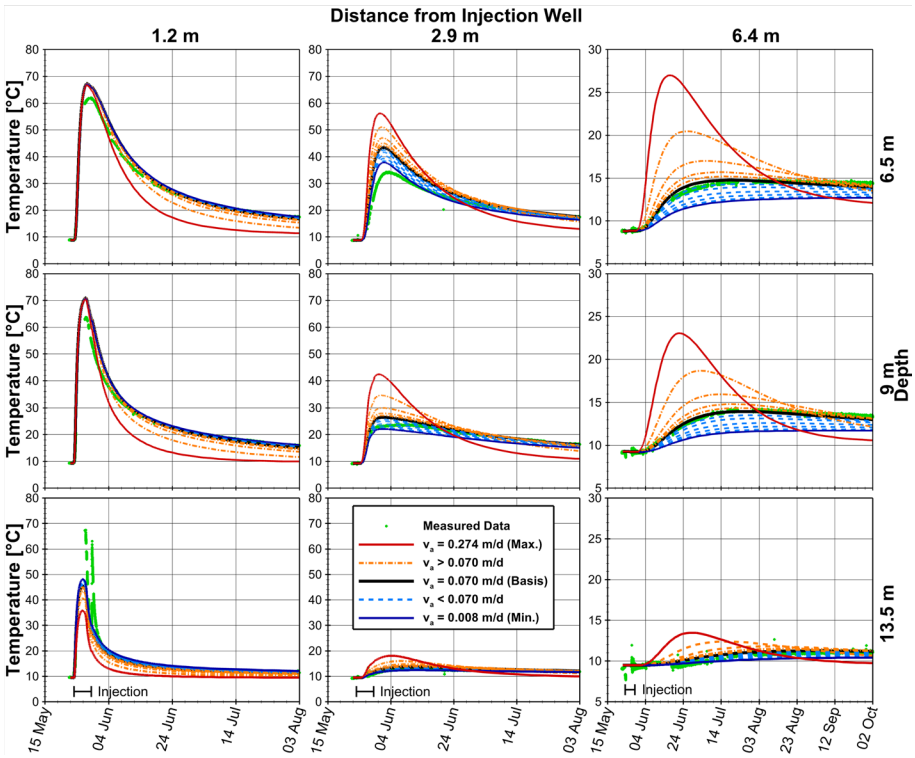

Fig. 12 Measured (green) and simulated temperature breakthrough curves for varied groundwater flow velocity v_a, shown for different depths and distances to the injection well. Measured temperatures are obtained from the same wells as in Fig. 3, temperature as well as time axis are rescaled for the right-hand side column. The black line indicates the base case, the blue lines indicate the scenarios with decreased v_a and the orange/red lines indicate the scenarios with increased v_a. The maximum and minimum scenarios, as derived from the literature, are displayed as the solid red and solid blue line, respectively, while the remaining sensitivity scenarios are displayed as dashed or dash-dotted lines

Abbreviations

CI	Circle inside
CM	Circle middle
CO	Circle outside
(HT- / LT-) ATES	(High-temperature/low-temperature) aquifer thermal energy storage
HIT	Heat injection test
NMAE	Normalized Mean Average Error
OGS	OpenGeoSys

List of symbols

c	Specific heat capacity [J/kg/K]
cρ	Volumetric heat capacity [J/m^3/K]
D_H	Heat conduction–dispersion tensor [W/m/K]
g	Vector of gravitational acceleration [m/s^2]
K	Intrinsic permeability tensor [m^2]
k_f^h	Horizontal hydraulic conductivity [m/s]
k_f^v	Vertical hydraulic conductivity [m/s]
n	Porosity [-]
p	Pressure [Pa]
Q_T	Heat source/sink term [J/m^3/s]
Q_w	Water source/sink term [1/s]
S	Specific storativity [1/Pa]
S_0	Specific storage [1/m]
T	Temperature [K]
t	Time [s]
v	Water flow velocity vector [m/s]
v_a	Groundwater flow velocity [m/d]

α	Aquifer compressibility [1/Pa]
β	Water compressibility [1/Pa]
β_l	Longitudinal thermal dispersivity [m]
β_t	Transversal thermal dispersivity [m]
δ_{ij}	Kronecker Delta [-]
λ	Thermal conductivity [W/m/K]
μ_w	Dynamic viscosity [Pa*s]
ρ	Density [kg/m^3]

Subscripts

s	Solid phase
w	Water

Acknowledgements
The authors thank Götz Hornbruch and Klas Lüders for setting up the test site infrastructure and being responsible for the largest part of the planning, construction and administration as well as experimental performance for the HIT reported herein and as representative for the whole TestUM project staff of Kiel University (CAU), as well as the Helmholtz Centre for Environmental Research (UFZ) Leipzig for geophysical exploration and installation of the monitoring wells. We thank all technicians, student assistants, and researchers supporting the field activities, Linwei Hu for providing the pumping test data, and the Kompetenzzentrum Geo-Energie of Kiel University (KGE) for co-funding. We further acknowledge the support by the municipality of Wittstock/Dosse and the Brandenburgische Boden GmbH.

Author contributions
SH: data curation, formal analysis, investigation, software, visualization, writing—original draft, writing—review and editing. BW: software, writing—original draft, writing—review and editing. SB: conceptualization, funding acquisition, writing—original draft, writing—review and editing. All authors read and approved the final manuscript.

Funding
Open Access funding enabled and organized by Projekt DEAL. This work was supported by the German Ministry of Economy and Climate Protection (BMWK) [Grant Number 03EWR006SD]; the German Ministry of Education and Research (BMBF) [Grant Number 03G0875A + B]; and the Project Management Jülich (PTJ).

Availability of data and materials
The datasets used and/or analyzed during the current study are available from the corresponding author on reasonable request.

Declarations

Competing interests
The authors declare that they have no competing interests.

Received: 7 July 2022 Accepted: 13 April 2023
Published online: 14 May 2023

References

Bauer S, Dahmke A, Kolditz O. Subsurface energy storage: geological storage of renewable energy—capacities, induced effects and implications. Environ Earth Sci. 2017;76:1–4. https://doi.org/10.1007/s12665-017-7007-9.
Bear J, Bachmat Y. Introduction to modeling and transport phenomena in porous media. Dordrecht: Kluwer; 1990.
Bloemendal M, Hartog N. Analysis of the impact of storage conditions on the thermal recovery efficiency of low-temperature ATES systems. Geothermics. 2018;71:306–19. https://doi.org/10.1016/j.geothermics.2017.10.009.
Boockmeyer A, Bauer S. High-temperature heat storage in geological media: high-resolution simulation of near-borehole processes. Geotech Lett. 2014;4:151–6. https://doi.org/10.1680/geolett.13.00060.
Bridger DW, Allen DM. Heat transport simulations in a heterogeneous aquifer used for aquifer thermal energy storage (ATES). Can Geotech J. 2010;47:96–115. https://doi.org/10.1139/T09-078.
Bridger DW, Allen DM. Influence of geologic layering on heat transport and storage in an aquifer thermal energy storage system. Hydrogeol J. 2014;22:233–50. https://doi.org/10.1007/s10040-013-1049-1.
Collignon M, Klemetsdal ØS, Møyner O, Alcanié M, Rinaldi AP, Nilsen H, Lupi M. Evaluating thermal losses and storage capacity in high-temperature aquifer thermal energy storage (HT-ATES) systems with well operating limits: insights from a study-case in the Greater Geneva Basin, Switzerland. Geothermics. 2020. https://doi.org/10.1016/j.geothermics.2019.101773.
Dahmke A, Hornbruch G, Lüders K, Bauer S, Hu L, Dietrich P, Werban U, Birnstengel S, Richnow H-H, Vogt C, Keller N-S, Geistlinger H, Zulfiqar B. Verbundprojekt UG: "TestUM-Aqiufer - Testfeld zur Untersuchung und zum Monitoring durch die Nutzung des Untergrundes induzierter reaktiver Mehrphasentransportprozesse in oberflächennahen Aquiferen": Abschlussbericht : Projektlaufzeit: 07/2017-10/2020. Kiel: Christian-Albrechts-Universität zu Kiel; 2021.
Decagon Devices. KD2 Pro thermal properties analyzer operator's manual. Pullman: Decagon Devices Inc; 2011.
Dinçer İ, Rosen MA. Thermal energy storage systems and applications. Chichester, United Kingdom: John Wiley & Sons Ltd; 2011.

Domenico PA, Schwartz FW. Physical and chemical hydrogeology. New York: John Wiley & Sons; 1990.
Dougherty DE, Babu DK. Flow to a partially penetrating well in a double-porosity reservoir. Water Resour Res. 1984. https://doi.org/10.1029/WR020i008p01116.
Fleuchaus P, Godschalk B, Stober I, Blum P. Worldwide application of aquifer thermal energy storage—a review. Renew Sustain Energy Rev. 2018;94:861–76. https://doi.org/10.1016/j.rser.2018.06.057.
Freeze RA, Cherry JA. Groundwater. New Jersey: Prentice-Hall Inc; 1979.
Gao L, Zhao J, An Q, Liu X, Du Y. Thermal performance of medium-to-high-temperature aquifer thermal energy storage systems. Appl Therm Eng. 2019;146:898–909. https://doi.org/10.1016/j.applthermaleng.2018.09.104.
Heldt S, Wang B, Hu L, Hornbruch G, Lüders K, Werban U, Bauer S. Numerical investigation of a high temperature heat injection test. J Hydrol. 2021a. https://doi.org/10.1016/j.jhydrol.2021.126229.
Heldt S, Wang B, Hu L, Hornbruch G, Lüders K, Werban U, Bauer S. Data of a high temperature heat injection test. Data Br. 2021b;36:107035. https://doi.org/10.1016/j.dib.2021.107035.
Hölting B, Coldewey WG. Hydrogeologie. Berlin, Heidelberg: Springer; 2013. https://doi.org/10.1007/978-3-8274-2354-2.
Hu L, Schnackenberg M, Hornbruch G, Lüders K, Pfeiffer WT, Werban U, Bauer S. Cross-well multilevel pumping tests – A novel approach for characterizing the changes of hydraulic properties during gas storage in shallow aquifers. J Hydrol. 2023; 620:129520. https://doi.org/10.1016/j.jhydrol.2023.129520
Janssen PHM, Heuberger PSC. Calibration of process-oriented models. Ecol Modell. 1995;83:55–66. https://doi.org/10.1016/0304-3800(95)00084-9.
Jeon JS, Lee SR, Pasquinelli L, Fabricius IL. Sensitivity analysis of recovery efficiency in high-temperature aquifer thermal energy storage with single well. Energy. 2015;90:1349–59. https://doi.org/10.1016/j.energy.2015.06.079.
Kabuth A, Dahmke A, Beyer C, Bilke L, Dethlefsen F, Dietrich P, Duttmann R, Ebert M, Feeser V, Görke UJ, Köber R, Rabbel W, Schanz T, Schäfer D, Würdemann H, Bauer S. Energy storage in the geological subsurface: dimensioning, risk analysis and spatial planning: the ANGUS+ project. Environ Earth Sci. 2017. https://doi.org/10.1007/s12665-016-6319-5.
Keller N-S, Hornbruch G, Lüders K, Werban U, Vogt C, Kallies R, Dahmke A, Richnow HH. Monitoring of the effects of a temporally limited heat stress on microbial communities in a shallow aquifer. Sci Total Environ. 2021;781:146377. https://doi.org/10.1016/j.scitotenv.2021.146377.
Kolditz O, Bauer S. A process-oriented approach to computing multi-field problems in porous media. J Hydroinformatics. 2004;6:225–44. https://doi.org/10.2166/hydro.2004.0017.
Kolditz O, Bauer S, Bilke L, Böttcher N, Delfs JO, Fischer T, Görke UJ, Kalbacher T, Kosakowski G, McDermott CI, Park CH, Radu F, Rink K, Shao H, Shao HB, Sun F, Sun YY, Singh AK, Taron J, Walther M, Wang W, Watanabe N, Wu Y, Xie M, Xu W, Zehner B. OpenGeoSys: an open-source initiative for numerical simulation of thermo-hydro-mechanical/chemical (THM/C) processes in porous media. Environ Earth Sci. 2012;67:589–99. https://doi.org/10.1007/s12665-012-1546-x.
Krol MM, Johnson RL, Sleep BE. An analysis of a mixed convection associated with thermal heating in contaminated porous media. Sci Total Environ. 2014;499:7–17. https://doi.org/10.1016/j.scitotenv.2014.08.028.
Lüders K, Hornbruch G, Zarrabi N, Heldt S, Dahmke A, Köber R. Predictability of initial hydrogeochemical effects induced by short-term infiltration of ∼75°C hot water into a shallow glaciogenic aquifer. Water Res X. 2021;13:100121. https://doi.org/10.1016/j.wroa.2021.100121.
Meng B, Vienken T, Kolditz O, Shao H. Evaluating the thermal impacts and sustainability of intensive shallow geothermal utilization on a neighborhood scale: lessons learned from a case study. Energy Convers Manag. 2019;199:111913. https://doi.org/10.1016/J.ENCONMAN.2019.111913.
Molson JW, Frind EO, Palmer CD. thermal energy storage in an unconfined aquifer: 2. model development, validation, and application. Water Resour Res. 1992;28:2857–67.
Molz FJ, Melville JG, Güven O, Parr AD. Aquifer thermal energy storage: an attempt to counter free thermal convection. Water Resour Res. 1983;19:922–30. https://doi.org/10.1029/WR019i004p00922.
Nendel C, Berg M, Kersebaum KC, Mirschel W, Specka X, Wegehenkel M, Wenkel KO, Wieland R. The MONICA model: testing predictability for crop growth, soil moisture and nitrogen dynamics. Ecol Modell. 2011;222:1614–25. https://doi.org/10.1016/j.ecolmodel.2011.02.018.
Nield DA, Bejan A. Convection in porous media. 4th ed. New York: Springer; 2013.
Nielsen JE, Vangkilde-Pedersen T. Underground Thermal Energy Storage (UTES) – general specifications and design. HEATSTORE project report. Geotherm. – ERA NET Cofund Geotherm; 2019.
Otto R. Zur Abschätzung von Wärmeleitfähigkeiten der oberflächennahen Lockergesteinsschichtenfolge in Norddeutschland. Grundwasser. 2012;17:219–29. https://doi.org/10.1007/s00767-012-0205-1.
Palmer CD, Blowes DW, Frind EO, Molson JW. Thermal energy storage in an unconfined aquifer: 1. Field injection experiment. Water Resour Res. 1992;28:2845–56. https://doi.org/10.1029/92WR01471.
Peter A, Dahmke A, Hornbruch G, Dietrich P, Werban U, Lamert H, Richnow HH, Vogt C, Schulz A, Geistlinger H, Lazik D, Großmann J, Beyer, Schreiber B, Heinrich B. Verbundprojekt UR II:„CO2-Leckage". CO2- Leckageversuch in einem oberflächennahen Grundwasserleiter zur Erprobung von Monitoringkonzepten und –methoden. Abschlussbericht zum Forschungsvorhaben 03G0670A-C; 2012a.
Peter A, Lamert H, Beyer M, Hornbruch G, Heinrich B, Schulz A, Geistlinger H, Schreiber B, Dietrich P, Werban U, Vogt C, Richnow HH, Großmann J, Dahmke A. Investigation of the geochemical impact of CO2 on shallow groundwater: design and implementation of a CO2 injection test in Northeast Germany. Environ Earth Sci. 2012b;67:335–49. https://doi.org/10.1007/s12665-012-1700-5.
Physikalisch-Technische Bundesanstalt, 1994. Mitteilung PTB-A 13.6. Braunschweig and Berlin.
Rakhshandehroo G, Akbari H, Afshari Igder M, Ostadzadeh E. Long-term groundwater-level forecasting in shallow and deep wells using wavelet neural networks trained by an improved harmony search algorithm. J Hydrol Eng. 2018;23:04017058. https://doi.org/10.1061/(asce)he.1943-5584.0001591.
REN21, 2016. Renewables 2016 Global Status Report, Renewables 2016 Global Status Report. ISBN 978–3–9818107–0–7
Schout G, Drijver B, Gutierrez-Neri M, Schotting R. Analysis of recovery efficiency in high-temperature aquifer thermal energy storage: a Rayleigh-based method. Hydrogeol J. 2014;22:281–91. https://doi.org/10.1007/s10040-013-1050-8.

Sheldon HA, Wilkins A, Green CP. Recovery efficiency in high-temperature aquifer thermal energy storage systems. Geothermics. 2021;96:102173. https://doi.org/10.1016/j.geothermics.2021.102173.
Todd DK. Groundwater hydrology. 2nd ed. New York: John Wiley & Sons; 1980.
Verein Deutscher Ingenieure, 2010. VDI 4640. Thermische Nutzung des Untergrundes. Düsseldorf.
Visser PW, Kooi H, Stuyfzand PJ. The thermal impact of aquifer thermal energy storage (ATES) systems: a case study in the Netherlands, combining monitoring and modeling. Hydrogeol J. 2015;23:507–32. https://doi.org/10.1007/s10040-014-1224-z.
Wang B, Bauer S. Converting heterogeneous complex geological models to consistent finite element models: methods, development, and application to deep geothermal reservoir operation. Environ Earth Sci. 2016. https://doi.org/10.1007/s12665-016-6138-8.
Yaws CL. Chemical properties handbook. New York: McGraw-Hill; 1995.

Publisher's Note